Q. J. R. Meteorol. Soc. (2001), **127**, pp. 1277–1292

Filtered non-hydrostatic models in pressure-related coordinates

By REIN RÕÕM[1]*, PEDRO M. A. MIRANDA[2] and ALAN J. THORPE[3]

[1]*Tartu Observatory, Estonia*
[2]*University of Lisbon, Portugal*
[3]*Met Office Hadley Centre, UK*

(Received 12 September 2000; revised 6 February 2001)

SUMMARY

The anelastic sigma-coordinate version of the pseudo-anelastic Miller–Pearce model is developed. The pseudo-anelastic model is characterized by the presence of external-mode acoustic perturbations which propagate in the horizontal, compromising the model performance by the need to use smaller time steps than would otherwise be required. The approach developed in this study allows for the filtering of acoustic waves and adjustment of surface pressure perturbations. The approach is tested in a new numerical implementation of an adiabatic sigma-coordinate non-hydrostatic model and results are found to be comparable to the unadjusted version, and to theory when applicable. The new code is found to allow for significantly larger time steps whilst still retaining numerical stability, showing the possibility of further model improvements.

KEYWORDS: Lamb waves Non-hydrostatic modelling Sigma-coordinate

1. INTRODUCTION

The use of pressure as the vertical coordinate in atmospheric dynamics was proposed by Eliassen (1949) and soon became the preferred choice in most large-scale studies, either in the pressure-coordinate (p-coordinate) form or in the sigma-coordinate (σ-coordinate) form. The latter was introduced by Phillips (1957) and allows for an implicit representation of surface orography. There are some good reasons for the popularity of p-space in atmospheric dynamics. The most obvious reason is that most atmospheric measurements are made in terms of pressure, and traditional meteorological analysis of the atmosphere is related to constant-pressure surfaces, whereas geometrical height, z, is a computed quantity. More important though, is the fact that the equations simplify in p-space, especially because the atmosphere is non-divergent in that framework. There are also some advantages in the formulation of the thermodynamic relationships in this context. In the case of hydrostatic dynamics, which are still dominant in meteorological theory and numerical applications at the large scale, these advantages have made the p-space very attractive.

The increasing resolution of both numerical forecast and climate models, as well as the growing requirements for model precision, has brought the transition from hydrostatic (HS) to non-hydrostatic (NH) models into the limelight. The development of non-hydrostatic models has been going on for about three decades, in the context of different mesoscale investigations (e.g. Ogura and Charney 1962; Dutton and Fichtl 1969; Miller and Pearce 1974; Tapp and White 1976; Klemp and Wilhelmson 1978; Redelsperger and Sommeria 1981; Pielke 1984), but NH models are still mostly used for research and for high-resolution or specialized studies, while operational forecasts rely on HS models. However, in the next five to ten years most HS models are likely to be replaced or updated to NH versions and there would be many advantages if the model upgrading could preserve connections with existing models and analysis tools, as well as with the forecasters' experience. These are all based on p-coordinate models.

Three main groups of NH p-space models have been developed:

* Corresponding author: Tartu Observatory, Tõravere, Tartuma 61602, Estonia.

(i) Models which employ the actual pressure of an air particle as the vertical coordinate (Miller 1974; Miller and Pearce 1974; Miller and White 1984; White 1989; Rõõm 1989, 1990).

(ii) Models which employ the hydrostatic component of the pressure field as the vertical coordinate (Laprise 1992): this coordinate system is used for instance in the Météo-France operational limited-area model, ALADIN (Bubnova *et al.* 1995).

(iii) Models which use the hydrostatic mean background pressure field as the vertical coordinate. This coordinate frame is employed in the NH extension of the Penn State–National Center for Atmospheric Research model (Dudhia 1993).

The first and probably best known NH model in pressure space is the Pseudo-anelastic Model (PAM, our terminology), introduced by Miller and Pearce (Miller 1974; Miller and Pearce 1974). A more general form of the PAM in pressure coordinates was presented by White (1989). The σ-coordinate versions of the PAM were developed by Miller and White (1984) and have been used in numerical modelling in the two-dimensional (2D) case by Xue and Thorpe (1991), and in the three-dimensional (3D) case by Miranda and James (1992) and Miranda and Valente (1997). The PAM abandons the hydrostatic equilibrium assumption in favour of the more exact vertical momentum equation but introduces, from scale-analysis arguments, the non-divergence of motion in p-space and this filters out the internal acoustic waves. The horizontally propagating external mode acoustic waves—Lamb waves (first described by Lamb (1932))—are maintained unless appropriate boundary conditions are used (Moncrieff and Miller 1976; Miller and White 1984). After both the internal and external acoustic modes are eliminated, the PAM becomes equivalent in essential details to the anelastic approximation in geometric space, in which the acoustic mode is completely eliminated by the assumption of a time-independent density distribution.

In this paper we will introduce a modified PAM, in the form of a novel σ-coordinate model NHAD (non-hydrostatic adjusted dynamics). The NHAD model is a modification of the earlier model, NH3D (Miranda and James 1992), the NH3D model is also a numerical realization of the PAM, but with the external mode included. The essential modification in the new model consists of the elimination of the external acoustic mode (in addition to elimination of the internal acoustic wave) for general flow over an uneven surface. For the simplest case, with no surface topography, the external acoustic mode can be eliminated by requiring the omega velocity to be zero on the bounding pressure surface (Moncrieff and Miller 1976), or by requiring the vertical velocity to be zero on the underlying surface (Miller and White 1984). Generalization of these ideas to the case of an uneven surface with orography is not straightforward because, to ensure mass conservation, appropriate boundary conditions on the horizontal boundaries for the non-hydrostatic geopotential equation need to be formulated. The NHAD model takes advantage of the acoustic filtering technique, first applied in the development of the non-hydrostatic High-Resolution Limited-Area Model (HIRLAM) (see Rõõm*; Männik and Rõõm†). However, in contrast to HIRLAM (which is a hybrid-coordinate model), in the NHAD model the upper boundary is chosen at a finite height, and lateral boundaries are considered transparent (radiative boundary conditions). These differences provide the NHAD model with distinctive properties and, thus, provide an opportunity to compare the influence of the coordinate system (σ-coordinates versus hybrid coordinates), and the lateral boundary conditions (radiative boundary versus absorbing layer) in p-coordinate-based models.

* http://apollo.aai.ee/HIRLAM/nhkern1.ps.gz (March 2000).
† http://apollo.aai.ee/HIRLAM/nhkern2.ps.gz (March 2000).

2. THE ANELASTIC SIGMA-COORDINATE MODEL

The main feature of the NHAD model is that the domain of integration is fixed in pressure coordinates, and the lower boundary of the domain is given by a fixed pressure distribution $p_0(\mathbf{x})$, independent of time:

$$p_{\text{top}} \leq p \leq p_0(\mathbf{x}).$$

Here p_{top} is the constant upper boundary. It is possible to choose $p_{\text{top}} = 0$, but, keeping the approach of the parent model NH3D, in this paper we assume $p_{\text{top}} > 0$. The pressure p_0 represents the mean background pressure at the surface, related to the topographic height by the barometric formula

$$p_0(\mathbf{x}) = p_s \exp\left(-\frac{g}{R}\int_0^{h(\mathbf{x})} \frac{\mathrm{d}z}{T_0(z)}\right),$$

where p_s is the mean sea-level pressure, R is the gas constant of dry air, g is the gravitational acceleration, T_0 represents the mean background temperature (elsewhere in this paper mean reference-state profiles are indicated by '0' suffixes), and $h(\mathbf{x})$ is the surface elevation. Let the σ-coordinate be defined as

$$\sigma = \frac{p - p_{\text{top}}}{p_*}, \tag{1}$$

where $p_*(\mathbf{x}) = p_0(\mathbf{x}) - p_{\text{top}}$. The fixed lower boundary requires a balance condition for the vertically integrated mass

$$\nabla \cdot \left(p_* \int_0^1 \mathbf{v}\, \mathrm{d}\sigma\right) = 0, \tag{2}$$

where $\mathbf{v}$ is the horizontal velocity vector $= (u, v)$. The fixing of the boundary p_0, along with application of condition (2), is the mechanism which eliminates external waves.

Except for the surface-pressure tendency equation, which is replaced by Eq. (2), the equations of motion in mass-conserving flux form are the same as in the NH3D model (Miranda and James 1992):

$$sw = -\dot{\sigma} - \sigma\frac{\dot{p}_*}{p_*}, \tag{3a}$$

$$\frac{\partial p_* w}{\partial t} + \hat{\mathcal{F}}_w = g p_* \left(\frac{\theta'}{\theta_0} + s\frac{\partial z'}{\partial \sigma}\right), \tag{3b}$$

$$\frac{\partial p_* \mathbf{v}}{\partial t} + \hat{\mathcal{F}}_{\mathbf{v}} = -g p_* \widehat{G} z' - f p_* \mathbf{k} \times \mathbf{v}, \tag{3c}$$

$$\frac{\partial p_* \theta'}{\partial t} + \hat{\mathcal{F}}_{\theta'} = -p_* \theta_0 \frac{N_0^2}{g} w + p_* Q, \tag{3d}$$

$$\widehat{G} \cdot (p_* \mathbf{v}) - \frac{\partial}{\partial \sigma}(s p_* w) = 0, \tag{3e}$$

where

$$\widehat{G} = \left(\nabla - \frac{\nabla p_*}{p_*}\sigma\frac{\partial}{\partial \sigma}\right)$$

is the horizontal p-coordinate gradient in the σ-coordinate representation. The geopotential height, z, and potential temperature, θ, are represented as sums of reference state

profiles z_0 and θ_0, depending on pressure only, and perturbation fields, represented by primed quantities. The Brunt–Väisälä frequency is indicated by N, and f is the Coriolis parameter. $\dot{\sigma}$ is the sigma velocity of an air parcel, Q represents the heat sources, ∇ is the gradient along a constant σ-surface and

$$\hat{\mathcal{F}}_\varphi = \frac{\partial}{\partial x}(p_* u\varphi) + \frac{\partial}{\partial y}(p_* v\varphi) + \frac{\partial}{\partial \sigma}(p_* \dot{\sigma}\varphi).$$

The vertical structure function, s, is defined as

$$s(\mathbf{x}, \sigma) \equiv \frac{g}{RT_0(p)} \frac{p}{p_*} = \frac{g}{R} \frac{\{\sigma + p_{\text{top}}/p_*(\mathbf{x})\}}{T_0\{\sigma p_*(\mathbf{x}) + p_{\text{top}}\}}.$$

The quantity w, defined in Eq. (3a), is an approximation of the vertical velocity, introduced by Miller and Pearce (1974), and $\dot{p}_*$ represents the material derivative of p_* at level σ:

$$\dot{p}_* = \mathbf{v}|_\sigma \nabla p_*. \tag{4}$$

Note that the temperature equation (3d) is not simplified, and represents potential-temperature conservation, $\mathrm{d}\theta/\mathrm{d}t = Q$, written here in flux form for the fluctuating part of potential temperature.

As Lamb waves have been eliminated, the actual surface pressure becomes adjusted, but not necessarily equal to the mean, time independent value, p_0. The actual surface-pressure fluctuation, p_0' (thus, the total pressure is $p_0 + p_0'$) can be evaluated from the geopotential-height fluctuation at the mean surface-pressure level, as:

$$\frac{p_0'}{p_*} = \frac{g z'_{\sigma=1}}{RT_0(p_0)}. \tag{5}$$

This formula is easy to prove by representing the total height, z, of the surface σ_s ($\sigma_s \neq 1$) as

$$z_{\sigma=\sigma_s} = z_{\sigma=1} + \left(\frac{\partial z}{\partial \sigma}\right)_{\sigma=1} (\sigma_s - 1),$$

and making use of relations

$$z'_{\sigma=1} = z_{\sigma=1} - z^{\text{mean}}_{\sigma=1},$$
$$z_{\sigma_s} = z^{\text{mean}}_{\sigma=1} = h$$

(where h is the elevation of the underlying surface),

$$\sigma_s - 1 = p_0'/p_*$$

and

$$(\partial z/\partial \sigma)_{\sigma=1} \approx RT_0(p_0)/g.$$

3. THE z-EQUATION

In all filtered NH models, cast in pressure-type coordinates, the geopotential height represents a diagnostic variable and its determination requires the solution of a non-homogeneous elliptical equation (z-equation), which is, in fact, a generalized Poisson equation. This is different from the exact dynamics, in which the geopotential height, z, represents a prognostic field (Rõõm 1998), and from the HS primitive-equation models,

in which z is a known function of surface pressure and temperature fields. Because the distribution of the geopotential height determines the distribution of the main forcing field in the system—the pressure-gradient force—its determination is a central task of every NH model and the z-equation represents the central relationship of every NH model.

The z-equation can be deduced by differentiating Eq. (3e) in time and eliminating time derivatives of the velocity components using the equations of motion (3b) and (3c)

$$\mathcal{L}z' + \mathcal{M}z' = A, \tag{6a}$$

where $\mathcal{L}$ and $\mathcal{M}$ are the horizontally homogeneous main operator and the horizontally non-homogeneous perturbation operator:

$$\mathcal{L} = \nabla^2 + \frac{\partial}{\partial\sigma}\bar{s}^2\frac{\partial}{\partial\sigma} \tag{6b}$$

$$\mathcal{M} = \frac{\partial}{\partial\sigma}\left\{\sigma^2\left(\frac{\nabla p_*}{p_*}\right)^2 + s'^2\right\}\frac{\partial}{\partial\sigma} - \frac{\nabla^2 p_*}{p_*}\sigma\frac{\partial}{\partial\sigma} - 2\frac{\nabla p_*}{p_*}\cdot\nabla\sigma\frac{\partial}{\partial\sigma}, \tag{6c}$$

A is a known function of velocity, temperature and surface pressure:

$$A = -\frac{1}{gp_*}\left[\left(\nabla - \frac{\nabla p_*}{p_*}\frac{\partial}{\partial\sigma}\sigma\right)\cdot(\mathcal{F}_\mathbf{v} + p_* f\mathbf{k}\times\mathbf{v}) - \frac{\partial}{\partial\sigma}\left\{\sigma\left(\mathcal{F}_w - gp_*\frac{T'}{T_0}\right)\right\}\right]$$

and $\bar{s}$, s' represent the horizontal mean and the fluctuation components of s:

$$s(\mathbf{x}, \sigma, t) = \bar{s}(\sigma, t) + s'(\mathbf{x}, \sigma, t), \quad \overline{s'} = 0.$$

A standard way for solving Eq. (6a) is to invert the main elliptical operator, $\mathcal{L}$, explicitly, and consider $\mathcal{M}$ iteratively (Xue 1989; Miranda 1991). This is possible because $\nabla p_*/p_* \approx -g\nabla h/(RT_0)$, and s', are small parameters in comparison with $\bar{s}$. At each iteration l, $l = 0, 1, 2, \ldots$, it is necessary to solve equation

$$\mathcal{L}z'^{(l)} = \mathcal{A}^{(l)}, \tag{7}$$

where $\mathcal{A}^{(l)} = A - \mathcal{M}z'^{(l-1)}$ is known from the previous iteration.

For the solution of Eq. (7), boundary conditions must be provided. At the lateral boundaries, the boundary values for z' are given, as in the parent model NH3D, from radiative boundary conditions, although, in some cases, it may be convenient to add a sponge region. Lateral sponges are found to be necessary in some nonlinear regimes, as a way of avoiding undesired changes in the upstream conditions, and in strongly non-hydrostatic backgrounds, for which the radiative boundary conditions may not work very well. However, the upper- and lower-boundary conditions in the adjusted model are, as first described by Rõõm*, novel.

At the upper boundary, $\sigma = 0$ ($p = p_{\text{top}}$), we need to apply a condition that eliminates solutions of the homogeneous equation $\mathcal{L}z' = 0$ which grow with height:

$$z' \to 0, \quad \text{if } \sigma \to 0 \quad \text{and} \quad \mathcal{A} \equiv 0. \tag{8}$$

Due to the elliptic nature of $\mathcal{L}$, the solution of Eq. (7) may include solutions of the homogeneous equation both exponentially growing and exponentially decreasing with height. The decreasing mode is caused by the lower-boundary condition, which is

* http://apollo.aai.ee/HIRLAM/nhkern1.ps.gz (March 2000).

equivalent to the existence of a surface source on the lower boundary. Similarly, the growing mode would be determined by the existence of some surface source on the upper boundary. As in reality there are no external sources at the top, the growing mode must be eliminated, and condition (8) for the homogeneous equation yields the absence of such a mode. The original *integrability condition*, formulated by Rõõm*, can not be applied here directly due to the finite height of the upper boundary. However, in a vertically discrete numerical model, the original *integrability condition* and Eq. (8) both yield the same elimination of undesired exponentially growing modes.

For the second 'vertical' constraint, the mass balance condition (2) is used. Differentiation of this condition in time yields

$$\nabla \cdot \left(g p_* \int_0^1 \widehat{G} z' \, \mathrm{d}\sigma \right) = -\nabla \cdot \int_0^1 (\hat{\mathcal{F}}_{\mathbf{v}} + f p_* \mathbf{k} \times \mathbf{v}) \, \mathrm{d}\sigma. \tag{9}$$

This 2D relationship replaces the usual lower Dirichlet condition (Xue and Thorpe 1991) of the unadjusted model. It guarantees that the initial mass-balance condition (2) holds for all time. Consequently, the lower-boundary value, $z_{\sigma=1}$, is not specified before Eq. (6a) is solved and, when the solution is found, this value determines, in accordance with Eq. (5), the adjusted surface-pressure fluctuation.

Numerical aspects of the inversion of Eq. (7) with conditions (8) and (9) with the use of eigenvector techniques are discussed in detail by Männik and Rõõm†.

4. THE NHAD MODEL AND NUMERICAL RESULTS

The proposed ideas have been applied in the development of the numerical model NHAD. Some results obtained with this new code are presented in this section and compared with the 'unadjusted' NH3D model, allowing for a discussion of the properties and performance of the new approach.

Model NHAD is a modification of the NH3D model (Miranda and James 1992). It includes the NH3D model as a special case, which can be switched on with a logical key. Most of the numerical implementation of the model and its main parameters are as described by Miranda and James (1992). The main differences between the NHAD model and the parent model NH3D are:

- In the NH3D model the lower-boundary p_* is prognosticated from the pressure-tendency equation. In the NHAD model it is fixed, and related to the surface elevation h, via the barometric formula

$$p_0 = a \exp\left(-\frac{g}{R} \int_0^h \frac{\mathrm{d}z}{T_0(z)} \right),$$

where a is the mean sea-level pressure, whereas the actual surface-pressure fluctuation is evaluated from Eq. (5).

- In the NH3D model, Dirichlet conditions are applied for z' at the upper and lower boundaries. In the NHAD model the upper- and lower-boundary values for z' are not fixed. Instead, conditions (8) and (9) are applied. Both models allow for spurious reflection of gravity waves from the top, though in the NHAD model the top reflection is reduced in comparison with the NH3D model due to the exclusion of spurious exponential modes of z' with the help of Eq. (8). To suppress reflection, a sponge layer is applied in both models.

* http://apollo.aai.ee/HIRLAM/nhkern1.ps.gz (March 2000).
† http://apollo.aai.ee/HIRLAM/nhkern2.ps.gz (March 2000).

• The NH3D model prognosticates vertical velocity from Eq. (3b). The NHAD model diagnoses vertical velocity from the equation

$$p_* s w = -\sigma \mathbf{v} \cdot \nabla p_* - \int_\sigma^1 \nabla \cdot (p_* \mathbf{v})\, d\sigma',$$

(this follows from Eq. (3e) with the help of Eq. (12)).

The modelling domain is a rectangular area in sigma space with dimensions $N_x \cdot \Delta x \times N_y \cdot \Delta y \times N_\sigma \cdot \Delta\sigma$. The model uses a staggered grid (Winninghoff 1968; Williams 1969), known in atmospheric dynamics as the Arakawa-C grid (Arakawa and Lamb 1977; Cullen 1991).

The time-integration scheme is an explicit leapfrog algorithm. For temporal smoothing, and for suppressing the decoupling tendency inherent in leapfrog schemes, an Asselin filtering technique (Robert 1966; Asselin 1972) is applied. Two spatial-filtering mechanisms are employed. A fourth-order filter is used to suppress short-scale instabilities with wavelengths $\approx$ two grid lengths. This filter was initially proposed by Durran and Klemp (1983) and generalized by Miranda (1991) to the 3D case. This filter is highly scale selective. All experiments that follow use a filter with very little impact on horizontal wavelengths larger then $2\Delta x$ and virtually no impact on the vertical structure. The spatial filter is applied once every five time steps. In the experiments shown in the following section, a sponge column was used near the lateral boundaries to guarantee the maintenance of the background conditions, in spite of the possible upstream influence associated with nonlinear regimes. That sponge affects the 10 grid points close to each lateral boundary. At the initial time the rigid-lid condition, $w|_0 = 0$, and vertically integrated mass balance Eq. (2) for the horizontal velocity $\mathbf{v}$ are assumed.

In the following experiments, the Coriolis force and moisture effects are left out (though the NH3D and NHAD models incorporate both of them), as having no relevance for surface-pressure adjustment and acoustic-relaxation processes.

(*a*) *Experiments with different flow regimes*

To test the new code, a set of numerical experiments were performed. Those experiments simulate the flow past an isolated bell-shaped circular mountain, and the flow parameters chosen—shown in Table 1—correspond to flow ($Na/U \gg 1$, where U is the advection velocity) in the three flow regimes identified by Miranda and James (1992)—quasi-linear mountain waves (Exp 1), splitting flow (Exp 2), and breaking waves (Exp 3)—and to one case of quasi-linear but strongly non-hydrostatic flow (Exp 4). For each experiment, two runs were performed with exactly the same parameters: one with the NH3D model, which is considered the control run, the other with the new NHAD code. All experiments use a $65 \times 65 \times 40$ grid-point grid, with 1 km horizontal resolution and variable vertical resolution implied by evenly spaced σ-surfaces, varying from about 200 m near the surface to about 1000 m near the top of the computational domain. All experiments used a time step of 2 s. The parameters were chosen so that the model is able to resolve both the main forced waves—with horizontal wavelength defined by the mountain shape—and the free oscillations, with wavelengths $2\pi U/N$.

The results obtained in Exp 1 are shown in Figs. 1, 2 and 3. Figure 1 shows the steady-state potential-temperature perturbation in the two simulations, which produce, for this and all other fields, almost identical distributions. The very slight differences between the two model results can also be appreciated in the evolution of the surface-pressure fluctuation and surface drag, presented in Figs. 2 and 3. The adjusted model yields, in comparison with the non-adjusted one, a slightly enhanced depression on

TABLE 1. NUMERICAL EXPERIMENTS

Experiment	h_0 (m)	U (m s^{-1})	N (s^{-1})	a (km)	dx (km)	Nh_0/U	Na/U
Exp 1 (Linear flow)	100	8	0.012	4	1	0.15	6
Exp 2 (Splitting)	2000	4.44	0.01	3	1	4.5	6.8
Exp 3 (Wave breaking)	1000	6.67	0.01	4	1	1.5	6
Exp 4 (Linear non-hydrostatic)	100	15	0.005	2	1	0.15	0.66

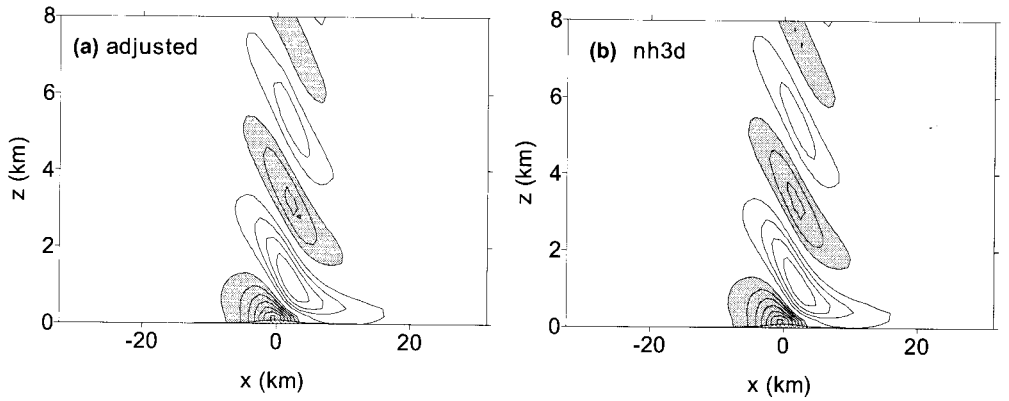

Figure 1. Potential-temperature perturbation at the central cross-section of the model in the steady-state case of Exp 1: (a) adjusted NHAD model; (b) NHD3 model. Contours shown: ±0.05, ±0.1, ±0.15, . . . , ±0.3 K. Shaded where $\theta' < -0.1$ K. See text for further explanation.

the lee side of the mountain (Fig. 2) and, consequently, enhanced downslope wind. Results of the modelling of surface drag are presented in Fig. 3. High-frequency oscillations of the unadjusted NH3D model during time steps 0–1000 mirror the initial adjustment process. The initial adjustment takes approximately 30 minutes in this particular example, which is ten times τ_L ($= L/c = (65\text{ km})/(350\text{ m s}^{-1}) \approx 3$ minutes). In spite of the fact that in the case of the adjusted model the surface drag is evaluated indirectly from the low-level geopotential perturbation, the results are virtually identical and converge to a numerical non-hydrostatic linear steady solution for the same grid (right y-axis). The results are also, in this case, very close to the hydrostatic analytical solution for the infinite bell-shaped mountain (left y-axis). Overall, the results seem to indicate the good behaviour of the new code.

Exp 2 corresponds to a regime of very high Nh_0/U, where horizontal streamline splitting around the mountain dominates the circulation. In this particular regime, as found by Smolarkiewicz and Rotunno (1989) and Miranda and James (1992), the flow tends to produce a pair of vortices, downstream of the mountain, with small amplitude mountain waves and reduced drag. Results for this experiment are shown in Fig. 4, showing the potential temperature, and Fig. 5, presenting the time evolution of the surface drag. Results are qualitatively similar, although the estimated drag shows somewhat higher values in the adjusted model. Because of that, the simulations were, in this particular case, extended to much higher values of non-dimensional time, to check the long-term behaviour of that flow, but the difference remained. On the other hand, an analysis of the different fields, including the vertical cross-sections and the surface flow, shown in Fig. 4, reveals only slight differences in the flow patterns, allowing the conclusion that the two models produce comparable results.

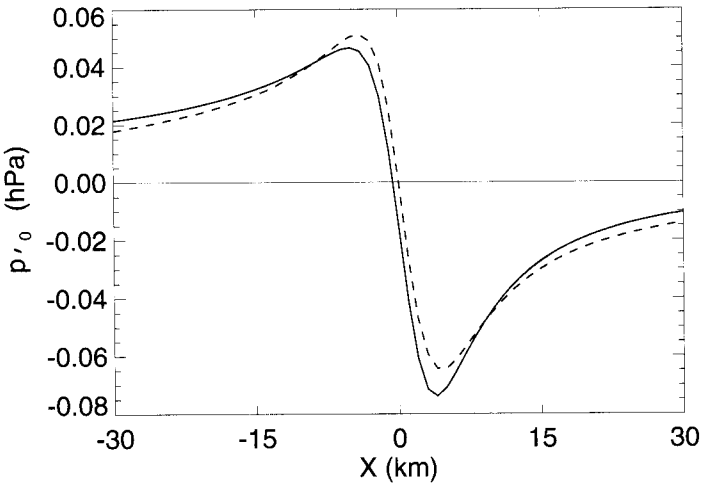

Figure 2. Surface pressure fluctuation (p_0') along the mountain x-axis in the asymptotically steady-flow regime for Exp 1, using the NH3D model (dashed line) and the adjusted NHAD model (solid line). See text for further explanation.

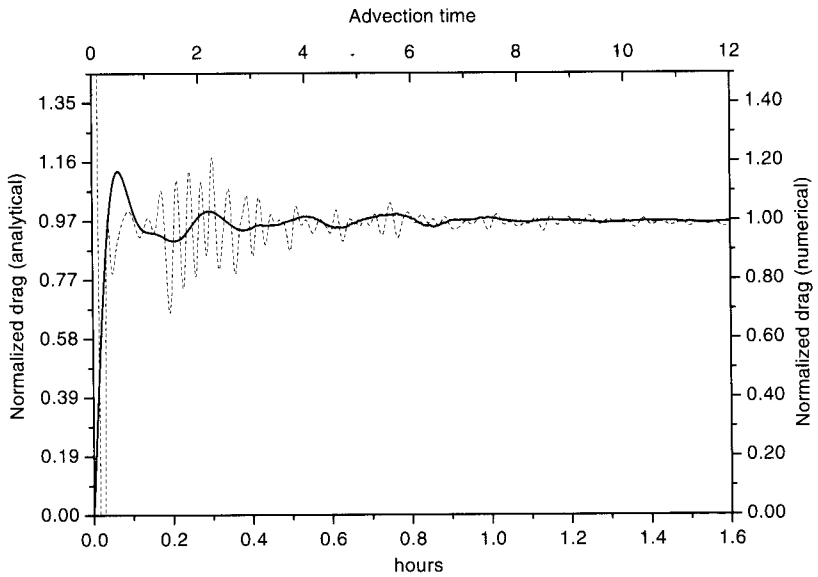

Figure 3. Time evolution of the normalized drag for Exp 1, using the NH3D model (dashed line) and the adjusted NHAD model (solid line). See text for further explanation.

Exp 3 corresponds to a value of the non-dimensional mountain height, $Nh_0/U = 1.5$, for which it has been found that wave breaking is likely to occur. In this case, it is expected that the flow will evolve into a transient regime, with oscillations in its behaviour associated with wave-breaking events. For that reason a direct comparison of results at a given time step, as done in the other cases, may be misleading. Instead, one must look at the general behaviour of the flow, and the time evolution of the drag is probably a good indicator of that behaviour. It is also known that in this case of wave-breaking flow, the solution depends on parameters other than the non-dimensional

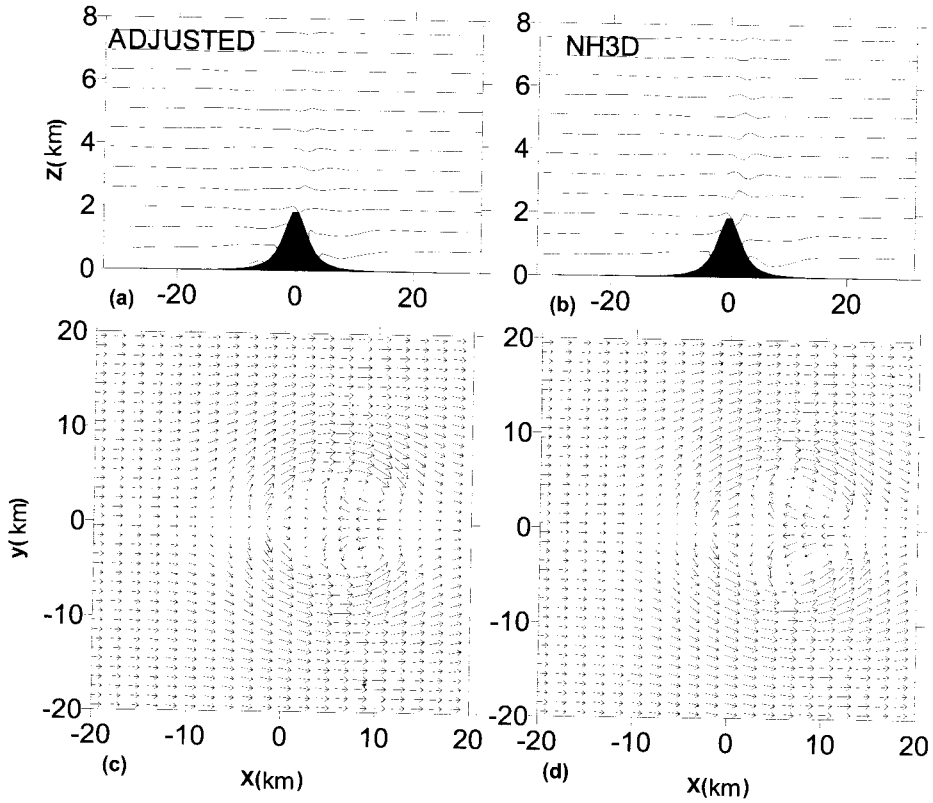

Figure 4. Potential temperature at the central cross-section of the model in the steady state of Exp 2: (a) NHAD model; (b) NH3D model. Contours shown every 1 K. Wind at the lowest model level: (c) NHAD model; (d) NH3D model. See text for further explanation.

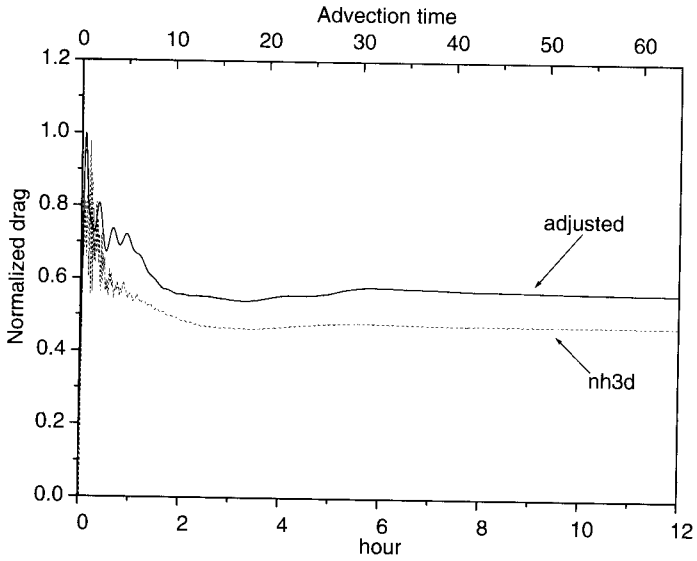

Figure 5. Time evolution of the normalized drag for Exp 2, using the NH3D model (dashed line) and the NHAD model (solid line). See text for further explanation.

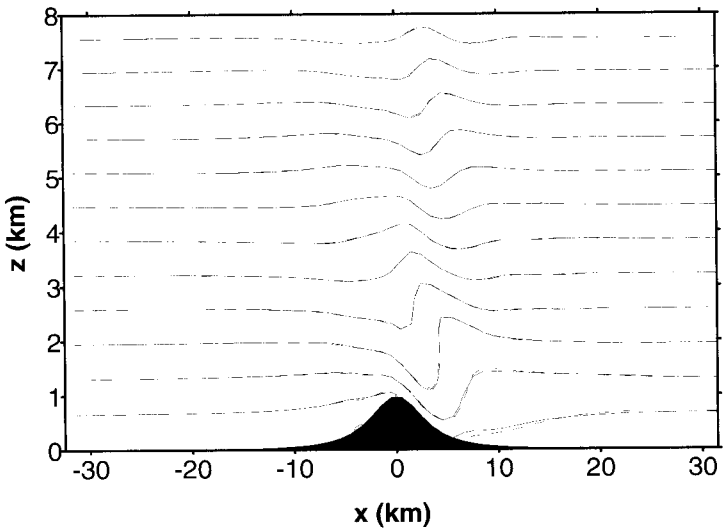

Figure 6. Potential temperature at the central cross-section of the model in the maximum-drag state of Exp 3 (3000 time steps, 1.75 h): NHAD (solid lines), NH3D (dashed). Contours every 2 K. See text for further explanation.

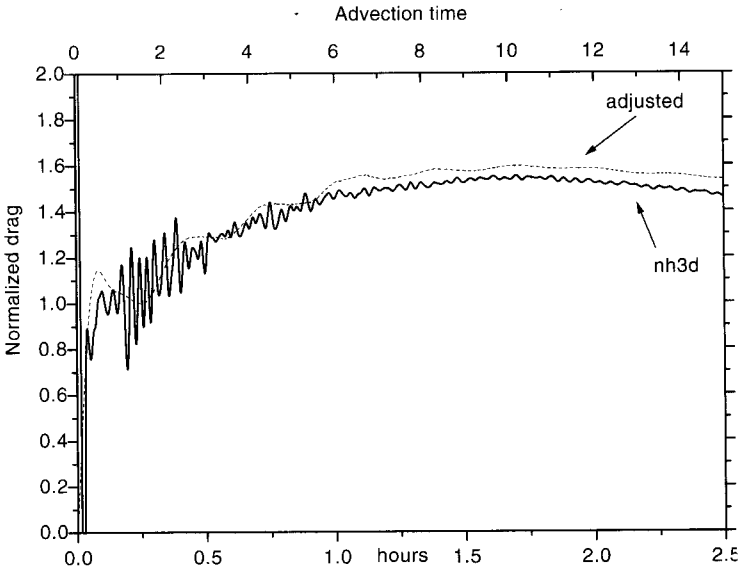

Figure 7. Time evolution of the normalized drag for Exp 3, using the NH3D model (solid line) and the NHAD adjusted model (dashed line). See text for further explanation.

mountain height (see Miranda and James 1992) and that there is a possibility of upstream-propagating modes changing the reference-state flow in time.

Results for Exp 3 are shown in Figs. 6 and 7. A comparison between the drag evolution curves (Fig. 7) indicates an excellent match between the two models. Looking at results at 3000 time steps, where the drag is at its maximum, the differences in flow structure are minimal. Both experiments show an almost identical vertical wave

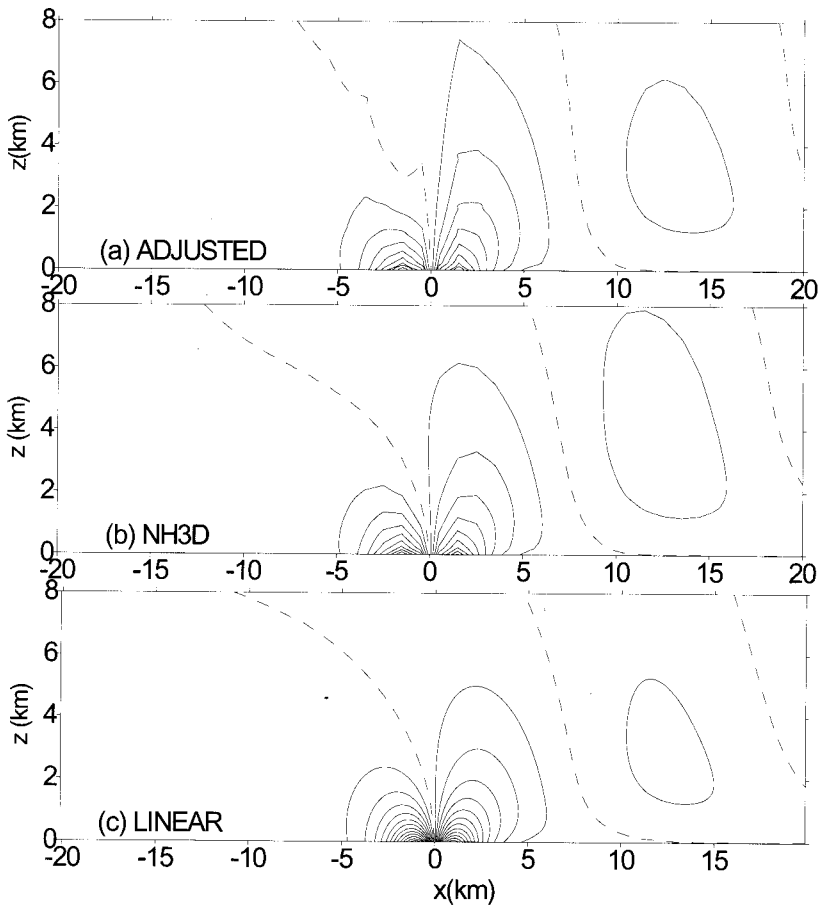

Figure 8. Vertical velocity in the steady state of Exp 4 for (a) the adjusted code , (b) NH3D and (c) the linear solution. Contours every 5 cm s^{-1}.

structure, with clear indications of large-amplitude mountain waves in a breaking regime. As expected, the behaviour of the NH3D model and of the NHAD code depend on different flow parameters and not just on the non-dimensional mountain height. Other experiments in the same wave-breaking regime ($Nh_0/U = 1.5$) but with different horizontal scale, showed drag evolution curves with different behaviours, and the match between NH3D and NHAD is not always as good as found in this particular case. In all cases, though, the qualitative behaviour is comparable, and the maximum values of the drag are similar.

The last experiment of this set, Exp 4, simulates a case of linear flow with $Na/U = 2/3$, for which non-hydrostatic effects are very strong. Figure 8 shows the vertical cross-section of the steady-state vertical velocity in this experiment, comparing the results from NH3D, NHAD (the adjusted code) and a linear model with the same parameters. As shown, the differences are minimal, indicating the good behaviour of both models in the simulation of this regime.

TABLE 2. STABILITY EXPERIMENTS

Parameters	Exp 5a NH3D/ADJ	Exp 5b NH3D/ADJ	Exp 5c NH3D/ADJ
h (m)	60	60	60
U (m s^{-1})	3	3	3
N (s^{-1})	0.005	0.005	0.005
a (km)	2	4	20
Δx (km)	1	2	20
Nh_0/U	0.1	0.1	0.1
Na/U	3.3	6.7	66.7
$\Delta t_{\max}$ (s)	8/100	10/140	35/165
C_i (m s^{-1})	1.6	3.2	32
$U\Delta t_{\max}/\Delta x$	0.024/0.3	0.015/0.21	0.005/0.025
$C_i\Delta t_{\max}/\Delta x$	0.013/0.16	0.016/0.22	0.056/0.26

(*b*) *Experiments on code stability*

Another set of experiments was performed to test the improvements in numerical stability gained with the NHAD code. These experiments correspond to a linear flow regime ($Nh_0/U = 0.1$), for which there is a well known solution. For each choice of parameters, a large number of experiments were performed with different time steps until it was found that numerical stability was destroyed. From those results, for each set of parameters, a maximum allowable time step is defined, which allows for the computation of the Courant number, $C\Delta t_{\max}/\Delta x$, where C is the propagation speed of perturbations in the flow. The propagation speed, C, depends on the advection velocity, U, and on the phase speed of the internal wave, C_i. The latter is a function of the horizontal scale and will have both horizontal and vertical components. As a consequence, two facts must be taken into account in the stability analysis:

(i) As the vertical resolution of the model is generally much larger than the horizontal resolution, especially in experiments with wide mountains, the relative importance of horizontal and vertical propagation will change with changes in horizontal resolution;

(ii) The relative importance of advection velocity and phase speed will also change with horizontal resolution.

Table 2 presents the parameters used in the three sets of simulations performed, one for each horizontal scale, and the obtained values of $\Delta t_{\max}$ for both the NH3D and NHAD code. In all experiments, the only difference in parameters between the two models is the value of the time step Δt, all other numerics being equal, including spatial and temporal smoothing, whereas diffusion was switched off.

An analysis of the data shown in Table 2 shows the large impact of the proposed approach, especially in the case of small horizontal scales, where changes in the maximum allowable time step were of an order of magnitude. The results also show that the gain in time step is a function of horizontal scale, because the phase speed of the waves increases with its horizontal wavelength and will dominate over the advection velocity above some value of the horizontal grid spacing. To clarify this effect, Table 2 shows a computation of the Courant number, $C\Delta t_{\max}/\Delta x$, from both the advection velocity and the phase speed of the internal wave for each experiment. Results obtained show that the new code runs in all three cases up to a Courant number of 0.2–0.3, an excellent result, typically an order of magnitude better than NH3D. This is a clear consequence of the removal of the Lamb wave. It should be mentioned though, that the time-step gains may be more modest when the permitted phase speeds are large

(comparable to the speed of sound) or when vertical propagation is the dominant effect in the definition of the Courant number, which is never the case in Exp 5a–c.

5. Conclusions

The main aim of this paper was to derive and test an anelastic σ-coordinate non-hydrostatic model filtering the external mode. The filtering was achieved by having a vertical domain of the model which is fixed in pressure coordinates, and deducing proper vertical boundary conditions for the non-hydrostatic geopotential-height equation. We have investigated the effect of using this set of equations to describe the dynamics of the atmosphere. Theoretical results were supported by the results of some numerical examples obtained with the NHAD model, which implements the proposed developments, compared with control experiments performed with the parent model NH3D.

Model results were found to be almost identical in the case of linear flow, for which there is a well known analytical result. In the two cases of highly nonlinear flow the two model formulations also produced very similar results, in the same regime and with similar surface drag, while the exact distributions of the different prognostic fields showed slight differences. Those differences were not much larger than those found between different numerical models or for the same model when changes are made to its numerical parameters (e.g. diffusion terms and spatial or temporal filtering).

An analysis of the numerical stability of the new formulation, made through a large set of experiments of flow past a small-amplitude mountain, proved the efficient removal of fast Lamb waves from the solution. The changes in the maximum allowable time step can be, in some cases, of one order of magnitude, approaching the theoretical limit for advection and/or maximum gravity-wave phase speed.

The use of the fixed geometry in p-space, as in this new formulation, increases computational accuracy, because it eliminates the fast Lamb waves in the solution. In this case, the surface-pressure fluctuation, which is not computed by the model, can be evaluated at every instant from the distribution of non-hydrostatic geopotential-height fluctuation at the time-mean surface-pressure level.

The conclusion then is that the new formulation of this pressure-based non-hydrostatic model is worth using and developing further.

Acknowledgement

P. Miranda had the financial support of the Portugese science funding program PRAXIS under Grant 3/3.2/EMG/1968/95. R. Rõõm had the financial support of the Estonian Science Foundation under Grant 2624 and from the Leverhulme Trust.

References

Arakawa, A. and Lamb, V. R. 1977 Computational design of the basic dynamical processes of the UCLA general circulation model. *Methods in Compt. Physics*, **17**, 174–265

Asselin, R. 1972 Frequency filter for time integration. *Mon. Weather Rev.*, **100**, 487–490

Bubnova, R., Hello, G., Benard, P. and Geleyn, J. F. 1995 Integration of the fully elastic equations cast in the hydrostatic pressure terrain-following coordinate in the framework of the ARPEGE/Aladin NWP system. *Mon. Weather Rev.*, **123**, 515–535

Cullen, M. J. P. 1991 Finite difference methods. Pp. 87–102 in *Numerical Methods in Atmospheric Models*. **1**. ECMWF, Reading, UK

Dudhia, J. 1993 A nonhydrostatic version of the Penn State–NCAR mesoscale model: Validation tests and simulation of an Atlantic cyclone and cold front. *Mon. Weather Rev.*, **121,** 1493–1513

Durran, D. R. and Klemp, J. B. 1983 A compressible model for the simulation of moist mountain waves. *Mon. Weather Rev.*, **111,** 2341–2361

Dutton, J. A. and Fichtl, G. H. 1969 Approximate equations of motion for gases and liquids. *J. Atmos. Sci.*, **26,** 241–254

Eliassen, A. 1949 The quasi-static equations of motion with pressure as independent variable. *Geofys. Publikasjoner (Oslo)*, **17,** 3

Klemp, J. B. and Durran, D. R. 1983 An upper boundary condition permitting internal gravity wave radiation in numerical mesoscale models. *Mon. Weather Rev.*, **111**, 430–444

Klemp, J. B. and Wilhelmson, R. B. 1978 The simulation of three-dimensional convective storm dynamics. *J. Atmos. Sci.*, **35,** 1070–1096

Lamb, H. 1932 *Hydrodynamics, 6th Edition.* Cambridge University Press, London, UK

Laprise, R. 1992 The Euler equations of motion with hydrostatic pressure as an independent variable. *Mon. Weather Rev.*, **120,** 197–207

Miller, M. J. 1974 On the use of pressure as vertical coordinate in modelling convection. *Q. J. R. Meteorol. Soc.*, **100,** 155–162

Miller, M. J. and Pearce, R. P. 1974 A three-dimensional primitive equation model of cumulonimbus convection. *Q. J. R. Meteorol. Soc.*, **100,** 133–154

Miller, M. J. and White, A. A. 1984 On the nonhydrostatic equations in pressure and sigma coordinates. *Q. J. R. Meteorol. Soc.*, **110,** 515–533

Miranda, P. M. A. 1991 Gravity waves and wave drag in flow past three-dimensional isolated mountains. PhD thesis, University of Reading

Miranda, P. M. A. and James, I. N. 1992 Non-linear three-dimensional effects on gravity-wave drag: Splitting flow and breaking waves. *Q. J. R. Meteorol. Soc.*, **118,** 1057–1081

Miranda, P. M. A. and Valente, M. A. 1997 Critical level resonance in three-dimensional flow past isolated mountains. *J. Atmos. Sci.*, **54,** 1574–1588

Moncrieff, M. W. and Miller, M. J. 1976 The dynamics and simulation of tropical cumulonimbus and squall lines. *Q. J. R. Meteorol. Soc.*, **102**, 373–394

Ogura, Y. and Charney, J. C. 1962 'A numerical model of thermal convection in the atmosphere'. Pp. 431–451 in Proceedings of the International symposium on numerical weather prediction, Tokyo. Meteorol. Soc. Jpn.

Phillips, N. A. 1957 A coordinate system having some special advantage for numerical forecasting. *J. Meteorol.*, **14,** 184–185

Pielke, R. A. 1984 *Mesoscale Meteorological Modeling.* Academic Press, San Diego, USA

Redelsperger, J. L. and Sommeria, G. 1981 Méthode de représentation de la turbulence d'échelle inférieure à la maille pour un modèle tri-dimensionnel de convection nuageuse. *Boundary-Layer Meteorol.*, **21,** 509–530

Robert, A. J. 1966 The integration of a low order spectral form of the primitive meteorological equations. *J. Meteorol. Soc. Jpn.*, **44,** 237–245

Rõõm, R. 1989 'The general form of dynamical equations of the atmosphere in the isobaric coordinate space'. Pp. 368–371 in Proceedings of the Estonian Academy Sci., Phys. Math., **38**

1998 Acoustic filtering in nonhydrostatic pressure coordinate dynamics: A variational approach. *J. Atmos. Sci.*, **55,** 654–668

1990 General form of the equations of atmospheric dynamics in isobaric coordinates. *Izvestiya, Atmospheric and Oceanic Physics*, **26,** 9–14

Smolarkiewicz, P. K. and Rotunno, R. 1989 Low Froude number flow past three-dimensional obstacles. Part I: Baroclinically generated lee vortices. *J. Atmos. Sci.*, **46,** 1154–1164

Tapp, M. C. and White, P. W. 1976 A nonhydrostatic mesoscale model. *Q. J. R. Meteorol. Soc.*, **102,** 277–296

White, A. A. 1989 An extended version of a non-hydrostatic, pressure coordinate model. *Q. J. R. Meteorol. Soc.*, **115,** 1243–1251

Williams, G. P. 1969 Numerical integration of the three-dimensional Navier-Stokes equations for incompressible flow. *J. Fluid Mech.*, **37**, 727–750

Winninghoff, F. J. 1968 'On the adjustment toward the geostrophic balance in a simple primitive equation model with application to the problems of initialization and objective analysis'. PhD thesis, University of California

Xue, M. 1989 'A nonhydrostatic numerical model in sigma-coordinates and simulations of mesoscale phenomena'. PhD thesis, University of Reading

Xue, M. and Thorpe, A. J. 1991 A mesoscale numerical model using the nonhydrostatic pressure-based sigma-coordinate equations: Model experiments with dry mountain flows. *Mon. Weather Rev.*, **119,** 1168–1185